Published in final edited form as:
NMR Biomed. 2013 December ; 26(12): 1853–1863. doi:10.1002/nbm.3039.

Quantitative susceptibility mapping of kidney inflammation and fibrosis in type 1 angiotensin receptor-deficient mice

Luke Xie[a,b], **Matthew A. Sparks**[c], **Wei Li**[d], **Yi Qi**[a], **Chunlei Liu**[a,d], **Thomas M. Coffman**[c], and **G. Allan Johnson**[a,d,*]

[a]Center for In Vivo Microscopy, Department of Radiology, Duke University Medical Center, Durham, NC, USA

[b]Department of Biomedical Engineering, Duke University, Durham, NC, USA

[c]Division of Nephrology, Department of Medicine, Duke University and Durham VA Medical Centers, Durham, NC, USA

[d]Brain Imaging and Analysis Center, Duke University Medical Center, Durham, NC, USA

Abstract

Disruption of the regulatory role of the kidneys leads to diverse renal pathologies; one major hallmark is inflammation and fibrosis. Conventional magnitude MRI has been used to study renal pathologies; however, the quantification or even detection of focal lesions caused by inflammation and fibrosis is challenging. We propose that quantitative susceptibility mapping (QSM) may be particularly sensitive for the identification of inflammation and fibrosis. In this study, we applied QSM in a mouse model deficient for angiotensin receptor type 1 (AT_1). This model is known for graded pathologies, including focal interstitial fibrosis, cortical inflammation, glomerulocysts and inner medullary hypoplasia. We acquired high-resolution MRI on kidneys from AT_1-deficient mice that were perfusion fixed with contrast agent. Two MR sequences were used (three-dimensional spin echo and gradient echo) to produce three image contrasts: T_1, T_2* (magnitude) and QSM. T_1 and T_2* (magnitude) images were acquired to segment major renal structures and to provide landmarks for the focal lesions of inflammation and fibrosis in the three-dimensional space. The volumes of major renal structures were measured to determine the relationship of the volumes to the degree of renal abnormalities and magnetic susceptibility values. Focal lesions were segmented from QSM images and were found to be closely associated with the major vessels. Susceptibilities were relatively more paramagnetic in wild-type mice: 1.46 ± 0.36 in the cortex, 2.14 ± 0.94 in the outer medulla and 2.10 ± 2.80 in the inner medulla (10^{-2} ppm). Susceptibilities were more diamagnetic in knockout mice: −7.68 ± 4.22 in the cortex, −11.46 ± 2.13 in the outer medulla and −7.57 ± 5.58 in the inner medulla (10^{-2} ppm). This result was consistent with the increase in diamagnetic content, e.g. proteins and lipids, associated with inflammation and fibrosis. Focal lesions were validated with conventional histology. QSM was very sensitive in detecting pathology caused by small focal inflammation and fibrosis. QSM offers a new MR contrast mechanism to study this common disease marker in the kidney.

*Correspondence to: G. A. Johnson, Center for In Vivo Microscopy, Department of Radiology, Duke University Medical Center, Box 3302, Durham, NC 27710, USA. gjohnson@duke.edu.

SUPPORTING INFORMATION

Supporting information may be found in the online version of this article.

Keywords

small animal preclinical imaging; magnetic susceptibility; quantitative susceptibility mapping; AT_1; renal structures; pathology; fibrosis; inflammation

INTRODUCTION

The major functions of the kidney include filtration, reabsorption, secretion and the generation of key hormonal mediators. The disruption of these regulatory roles leads to a diverse spectrum of renal diseases. One major hallmark of renal diseases is pathology caused by inflammation and fibrosis (1,2). Noninvasive imaging, especially MRI, has been essential in monitoring the onset and development of many renal diseases (3–5). However, the use of imaging to quantify or detect focal pathology caused by fibrosis remains a challenge (1,6,7). A relatively new MRI contrast mechanism based on magnetic susceptibility has provided a structural contrast, higher structural resolution and quantitative local information not seen in standard magnitude images (8–12). Magnetic susceptibility can be determined with a technique called quantitative susceptibility mapping (QSM) (13–17). We reasoned that QSM might be particularly sensitive for the detection and quantification of inflammation and fibrosis in the kidney parenchyma. We applied QSM to detect and quantify these renal pathological abnormalities in a mouse model deficient for angiotensin receptor type 1 (AT_1).

AT_1 mediates the classical hypertensive actions of the renin–angiotensin system and is a key hormonal regulator of kidney development. The mice used have targeted deletion of one or both murine AT_1 isoforms—AT_{1A} and AT_{1B}. Mice deficient in AT_{1A} (*Agtr1a*−/−) or combined AT_{1A} and AT_{1B} (*Agtr1a*−/− *Agtr1b*−/−) have a significantly blunted systemic pressor response to angiotensin II and reduced basal blood pressure (18). Moreover, combined AT_{1A} AT_{1B} deletion is characterized by significant changes in the kidney parenchyma. These abnormalities, which have been determined previously by standard pathological staining methods, include thickened arterial walls (19), focal areas of tubular dropout with interstitial fibrosis, cortical inflammation (18), glomerular cystic changes (20) and hypoplasia of the inner medulla (21–24). Subtle features of this phenotype can be seen in mice lacking only the major AT_1 isoform AT_{1A}. We applied this model because the focal lesions and subtle abnormalities require a sensitive and quantitative tool for detection.

We performed high-resolution MRI on perfusion-fixed kidneys from three animal cohorts: wild-type, AT_{1A} knockout and combined AT_{1A} and AT_{1B} knockout. Two MR sequences were used including a T_1-weighted spin echo and T_2*-weighted gradient echo. These sequences produced three different image contrasts: T_1, T_2* (magnitude) and QSM. The T_1 and T_2* (magnitude) image contrasts were acquired to segment the major renal structures and to provide landmarks and references for the focal lesions of inflammation and fibrosis in the three-dimensional space. The volumes of the major renal structures were measured to determine the relationship between these renal structures and the degree of inflammation and fibrosis, and the corresponding susceptibility values. Inflammation and fibrosis were validated with conventional histology.

METHODS

Biological support

All animal studies were performed at the Duke Center for In Vivo Microscopy and were approved by both the Duke and Durham VA Institutional Animal Care and Use Committees. Mice used in this study were C57BL/6 wild-type (n = 4, 4 months old), homozygotes for

disruption of the *Agtr1a* gene locus lacking AT_{1A} on the C57BL/6 background (n = 4, 4 months old) and compound homozygotes for disruption of *Agtr1a Agtr1b* loci lacking all AT_1 on a mixed background (n = 6, 4 months old). Targeted mutation of the angiotensin receptor genes has been described in detail elsewhere (18,25).

Animals were provided with free access to water before organ harvest. For tissue preservation and removal, mice were anesthetized with isoflurane, a midline abdominal incision was made and a 27-gauge needle was inserted into the heart. Transcardial perfusion fixation was used with inflow to the left ventricle and outflow from the right atrium. The animals were perfused with saline and 0.1% heparin flush, followed by a 50 mM ProHance (Gadoteridol, Bracco Diagnostics Inc., Princeton, NJ, USA) contrast agent dissolved in 10% formalin. Both saline and ProHance were perfused at 8 mL/min for 5 min using a perfusion pump. ProHance, a gadolinium-based contrast agent, was used as the active stain to decrease the T_1 relaxivity (26). The renal artery, vein and ureter were ligated and the kidney was excised from the animal. Immediately after perfusion, kidneys were immersed in 10% formalin to preserve the tissue. Kidneys were then immersed in a phosphate-buffered saline solution (10 mM) with 2.5 mM ProHance for 24 h before imaging. Specimens were stored in buffered solution to prevent dehydration (26). The weights of the kidneys were measured using an analytical balance after all imaging procedures.

Additional kidneys were prepared without contrast agent. The same perfusion fixation and immersion procedures were used but without the ProHance contrast agent. One kidney from each of the three cohorts was prepared and imaged (n = 1 for wild-type, n = 1 for *Agtr1a*−/− and n = 1 for *Agtr1a*−/− *Agtr1b*−/−).

MRI

MR images were acquired on a 9.4-T system (400-MHz vertical bore Oxford superconducting magnet) dedicated to magnetic resonance microscopy (27). The system consists of an 89-mm vertical bore magnet controlled by a GE Signa console (Epic 12 M5, GE Medical Systems, Milwaukee, WI, USA). Each kidney was fitted in an acrylic holder filled with fomblin (Ausimont USA, Inc., Thorofare, NJ, USA) to limit susceptibility artifacts at the surface of the tissue. The acrylic specimen holder was placed in a 13-mm (diameter) × 23-mm (length) solenoid radiofrequency coil. Contrast-enhanced specimens were scanned with a T_1-weighted spin echo sequence (flip angle, 90°; TR = 50 ms; TE = 5.2 ms) and a T_2*-weighted gradient echo sequence (flip angle, 60°; TR = 50 ms; TE = 4.4 ms). Additional kidneys without contrast agent (longer T_2*) were scanned with a T_2*-weighted multiecho gradient echo sequence (flip angle, 60°; TR = 500 ms; TE_1/spacing/TE_{10} = 4.4/4.9/48.9 ms), which enhanced the susceptibility signal-to-noise ratio (SNR) when individual echo images were summed (28). All images were acquired using a field of view of 16 × 8 × 16 mm^3 and a matrix size of 512 × 256 × 512, resulting in an isotropic resolution of 31 × 31 × 31 μm^3 (voxel volume, 30 pL). The dynamic range of the MR system was extended using a segmented acquisition to enhance the high frequencies of Fourier space (27). Specifically, the analog gain was set higher for the periphery of k space and was set lower for the center of k space. In both cases, the gain was set to fill at least 15 bits of the digitizer. Towards the center of k space, to avoid saturation of the digitizer, the analog gain was decreased in 6-dB steps. For each 6-dB step, the data sampling was doubled. This method both matches the signal level of the periphery of k space and increases the dynamic range towards the center.

QSM

Raw (Fourier) data from T_2*-weighted acquisitions were also used to reconstruct QSM images (15,16). The local phase in the data was extracted using a Laplacian-based three-

dimensional phase unwrapping algorithm. The background phase was removed with a sphere-mean-value filter with a kernel of 30 voxels and a kernel width decreasing towards the tissue boundary (15,29). The QSM was then calculated with a least-squares algorithm using orthogonal and right triangular decomposition by inverting the following equation (30,31):

$$f(r)=\mathrm{FT}^{-1}\left\{\left(\frac{1}{3}-\frac{k_z^2}{k^2}\right)\chi(k)\right\}\gamma\mu_0 H_0 \quad [1]$$

where $\chi(k)$ is the susceptibility map in the frequency domain, k is the reciprocal space vector and k_z is its z component, γ is the gyromagnetic ratio for a water proton, μ_0 is the vacuum permeability, H_0 is the magnitude of the main magnetic field, $f(r)$ is the frequency offset map and FT^{-1} is the inverse Fourier transform. The reconstruction process from the image phase to QSM is shown in Fig. 1. The QSM process for all three cohorts is shown in Fig. S1. Here, susceptibility based on Equation [1] is assumed to be isotropic; datasets were acquired at a single orientation with the magnetic field pointing along the mediolateral axis of the kidney. Thus, the susceptibility values measured are the apparent magnetic susceptibility (32). QSM is determined relative to the entire kidney, which was chosen as the reference tissue. Individual echo datasets from the multiecho sequence were processed to obtain QSM in the same manner. Individual QSM images were first corrected for the gyromagnetic ratio, permittivity of free space, magnetic field and TE, and thus are represented in parts per million of B_0. The corrected echo images were then summed to produce the final multiecho-enhanced QSM image. We assumed that the susceptibility-induced phase shift was linearly dependent on TE.

Susceptibility values were measured from regions of interest (ROIs) in each of the renal regions (cortex, outer medulla and inner medulla). Additional measurements were taken in the pelvis, a liquid-filled structure, to demonstrate the consistency of the susceptibility values. The ROIs were selected in limited areas, near the central slice of each kidney, and away from major vessels and cystic regions. In kidneys with contrast agent, mean and standard deviation values were determined from the susceptibilities across kidney samples within each cohort (n = 4 for wild-type, n = 4 for *Agtr1a*−/− and n = 6 for *Agtr1a*−/− *Agtr1b*−/−). In kidneys without contrast agent, mean and standard deviation values were determined from the susceptibilities within an ROI in a single kidney for each cohort (n = 1 for wild-type, n = 1 for *Agtr1a*−/− and n = 1 for *Agtr1a*−/− *Agtr1b*−/−). Susceptibility values are also provided for the renal regions relative to the pelvis.

Segmentation of major renal structures

The vasculature was segmented from T_1-weighted images using a region-growing operation with several seeds in Avizo software (Visualization Sciences Group, Burlington, MA, USA). Seeded region growing was based on a user-defined intensity range (lower and upper threshold) and a six-connectivity neighborhood. Arteries and veins were in separate compartments and were easily separated using seeded region growing. The segmented vasculature with determined nodes and branches (vessel segments) is shown in Fig. S2. The renal regions, including the cortex, outer medulla and inner medulla, were segmented from T_2*-weighted (magnitude) images. The regions were segmented using a dual thresholding process called hysteresis, which was completed using MATLAB (MathWorks Inc., Natick, MA, USA) and Avizo. The hysteresis process is shown in Fig. S3. The segmented renal structures were overlaid and confirmed on the MR image. The step-by-step method of isolating the renal structures is described in the segmentation process (see Supporting information). Measurements determined from the segmented structures included vessel

segment lengths and volumes of the cortex, outer medulla and inner medulla. The kidney volume was determined by summing the three renal regions.

Histology

MR images were validated with conventional histology of the same kidneys. The kidneys were sliced in the coronal plane, stored in 10% formalin, embedded in paraffin and sectioned at a thickness of 5 μm. Sections stained with hematoxylin and eosin (H&E) and Masson's Trichrome were obtained from adjacent central sections of the kidney. These slides were digitally scanned using bright-field contrast on an Axioskop 2 FS microscope (Carl Zeiss Microscopy, LCC, Thornwood, NY, USA). Images were acquired at 1.02 μm resolution using a 10× objective and were tiled to cover the entire kidney section. Images captured from bright-field microscopy exhibit shading effects that are apparent in tiled images. Shading correction was applied by removing a background image with no sample. MR images were manually registered to corrected histology images to enable comparison. H&E-stained slides were used to demonstrate the accuracy of the vasculature and renal region segmentation. Masson's Trichrome-stained slides were used to identify inflammation and fibrosis and to validate findings from QSM images.

Statistics

Statistical analysis was implemented in MATLAB. The mean QSM values were compared between cohorts ($n = 4$ for wild-type, $n = 4$ for *Agtr1a*−/− and $n = 6$ for *Agtr1a*−/− *Agtr1b*−/−). A two-tailed Student's *t*-test with unequal variances was used to test for significance. A significance level of 5% (unless otherwise noted) was used to reject the null hypothesis that the means of the metrics measured within a cohort were equal to the means from another cohort. This test was used between three cohort pairs: wild-type *versus Agtr1a*−/−, wild-type *versus Agtr1a*−/− *Agtr1b*−/− and *Agtr1a*−/− *versus Agtr1a*−/− *Agtr1b*−/−. All values in this study are reported as means ± standard deviation.

RESULTS

Figure 2 shows representative T_1-weighted images of kidneys from wild-type (Fig. 2A), *Agtr1a*−/− (Fig. 2B) and *Agtr1a*−/− *Agtr1b*−/− (Fig. 2C) mice. It should be noted that the isotropic resolution allows the interactive reslicing of the data to display the same anatomical landmarks – in this example, a slice that includes all of the major regions down to the papilla.

QSM

QSM relies on a contrast mechanism in MRI arising from local, microscopic variations in the magnetic field. In conventional T_2*-weighted (magnitude) images, these magnetic susceptibility variations frequently result in artifacts that blur some of the smaller details. We used QSM images to characterize the architecture of the renal cortex. Figure 3 compares the cortex in the wild-type (Fig. 3A–C) and *Agtr1a*−/− *Agtr1b*−/− (Fig. 3D–F) mice. The QSM images (Fig. 3C, F) were matched with the T_2*-weighted (magnitude) images (Fig. 3B, E) and Masson's Trichrome histology images (Fig. 3A, D). Areas of inflammation and fibrosis were identified (see yellow arrows in Fig. 3A, D). Kidneys from normal adult mice can have fibrosis as a result of spontaneous diseases, such as chronic progressive nephropathy, or pathology associated with aging (33). These areas appear dark in the magnitude image because of rapid T_2* relaxation, and are probably a result of reduced water content and increased susceptibility heterogeneity. Furthermore, this region of low signal intensity is artificially large because of the local field inhomogeneity, an effect known as 'blooming artifact'. The corresponding QSM image (Fig. 3C) shows negative magnetic susceptibility in the same region and restores the structural detail and resolution that were

compromised in the magnitude images. Glomerulocysts were identified in the *Agtr1a*−/− *Agtr1b*−/− mouse (see white arrows in Fig. 3D–F). Glomerular wall wrinkling, tufts and enlarged Bowman's space characterize glomerulocysts. Consequently, these areas showed high positive susceptibility because the vacuolated areas are filled with contrast agent, which is paramagnetic (Fig. 3F). The local field distortion again causes blurring in the magnitude image (Fig. 3E), which is removed in the QSM image. The areas with filled contrast agent, inflammation and fibrosis create diffuse and broad magnetic susceptibilities across the entire cortical region. These focal areas and clusters were much more prominent in the kidneys of *Agtr1a*−/− *Agtr1b*−/− mice than of wild-type mice.

Maximum intensity projections (MIPs) were constructed from T_2* magnitude and QSM images (from the same dataset) to enhance the comparison of structures in the cortical region. The cortex was the region of focus because of the structural changes found in the histology and QSM images. MIPs from QSM images highlighted finer structures in the cortex better than MIPs from magnitude images. Finer structures and vessels in the most outer cortical region were well defined in QSM images from wild-type and *Agtr1a*−/− mice (Fig. 4B, D). As one moves from the images of the wild-type and *Agtr1a*−/− mice to that of the *Agtr1a*−/− *Agtr1b*−/− mouse (Fig. 4F), the fine vasculature becomes less clear. These structures are still present in the kidneys from the *Agtr1a*−/− *Agtr1b*−/− mouse, but their visibility is confounded by the adjacent paramagnetic susceptibility content in glomerulocysts and the diamagnetic susceptibility content in areas of inflammation and fibrosis. These differences across the cohorts are less obvious in the magnitude MIPs (Fig. 4A, C, E).

QSM values were determined from ROIs in limited areas in the cortex, outer medulla, inner medulla and pelvis. The mean susceptibilities and standard deviations across tissue samples for each cohort are shown in Table 1. Additional QSM values relative to the pelvis were determined for each cohort. The number of pixels sampled in each ROI is included in Tables S1 and S2. Generally, the susceptibilities were more diamagnetic in the knockout cohorts and were significantly different between wild-type and *Agtr1a*−/−, wild-type and *Agtr1a*−/− *Agtr1b*−/−, and *Agtr1a*−/− and *Agtr1a*−/− *Agtr1b*−/− for the cortex, outer medulla and inner medulla. The exception was in the inner medulla, where the susceptibilities were not significantly different between *Agtr1a*−/− and *Agtr1a*−/− *Agtr1b*−/−. Susceptibility values in the pelvis were not significantly different between the cohorts. The standard deviation was highest in the *Agtr1a*−/− *Agtr1b*−/− cohort, which is consistent with Figs 3 and 4, where the inflammation and fibrosis give rise to increased heterogeneity in the first three renal regions. The variation is also much greater in the medullary regions compared with the cortex, which may be a result of the structural heterogeneity caused by hypoplasia.

QSM images of kidneys without contrast agent were also compared. Results were similar to the kidneys with contrast agent. MIPs were produced for one kidney in each cohort (Fig. 5). Fine vessels and structures were visible in the wild-type and *Agtr1a*−/− mice (Fig. 5A, B), but were less visible in the *Agtr1a*−/− *Agtr1b*−/− mouse (Fig. 5C). The visibility was also confounded because of increased glomerulocysts, inflammation and fibrosis. The mean susceptibilities and standard deviations were determined from ROIs for each cohort (Table 2). The number of pixels sampled in each ROI is included in Tables S3 and S4. The susceptibilities were more diamagnetic in the knockout cohorts in the cortex, outer medulla and inner medulla. Susceptibilities were more paramagnetic in the wild-type kidneys. Values in the pelvis were also consistent across the cohorts.

Inflammation, fibrosis and the major renal structures

The histology images (Fig. 3) also revealed that the vessels were closely associated with the focal lesions in the cortex. For this reason, we segmented the vasculature and renal cortex to

determine the proximity of the renal structures with inflammation and fibrosis in the three-dimensional space. The inner medulla and outer medulla were segmented to provide additional reference and landmarks for the focal lesions. The results of the segmented renal structures are shown in Fig. 6. T_1-weighted images were excellent for isolating the vasculature (Fig. 6A) and T_2*-weighted (magnitude) images were excellent for segmenting the renal regions (Fig. 6B). These segmentation results were inspected for accuracy with each MRI slice and matching H&E histology images. Isolated structures are shown for a wild-type mouse. The measurements of the renal structures of all three cohorts are shown in Fig. 7. The mass of the kidney specimen, which was measured by analytical balance, is included in Fig. 7A. The segmentation and additional measurements of the renal structures of all three cohorts are shown in Figs S4–S6.

Focal lesions of inflammation and fibrosis were segmented from the QSM images using simple thresholding at -39.8×10^{-2} ppm, which was determined by visual inspection. This threshold value was chosen in order to visualize some of the lesions in the three-dimensional space and to compare the spatial distribution between animal cohorts. The segmentation results viewed with the major renal structures are shown in Fig. 8. We found very limited fibrotic regions in the wild-typemouse and only displayed volume renderings from the *Agtr1a*−/− and *Agtr1a*−/− *Agtr1b*−/− mice. Susceptibility values in the segmented lesions were −48.5± 9.9 ppm (2) in *Agtr1a*−/− and −46.7 ± 7.3 ppm (2) in *Agtr1a*−/− *Agtr1b*−/− mice. There are two key findings from these results. First, the lesions are closely associated with the major cortical vessels (indicated by the yellow arrow in Fig. 8A, inset). Second, the extent of lesions in the cortex is greater in the kidney from the *Agtr1a*−/− *Agtr1b*−/− mouse (indicated by the yellow arrow in Fig. 8B, inset). Considering the reduced kidney and cortex size in the *Agtr1a*−/− *Agtr1b*−/− mouse, this fibrotic extension in the cortex was even more severe compared with that in the *Agtr1a*−/− mouse.

DISCUSSION

We have used QSM to study an AT_1-deficient mouse model noted for graded abnormalities. Kidneys deficient in AT_1 exhibited numerous malformations, most importantly inflammation and focal interstitial fibrosis. These focal lesions are subtle both in size and contrast, and can be much more difficult to detect than large structures, such as renal regions or major vessels. These structures were not clearly visible in the T_2*-weighted (magnitude) images. They were much more visible in the QSM images, and we were able to quantify changes in these small focal lesions. To the best of our knowledge, this study demonstrates the first QSM of fibrosis in the kidney.

QSM is an excellent contrast mechanism and is particularly sensitive to molecular content, cellular arrangement and tissue microstructure. When these contents are altered by disease, QSM can detect the differences and determine the source of contrast. The pathology in the disease model introduced many changes in the microstructure and molecular content. Kidneys from *Agtr1a*−/− *Agtr1b*−/− mice exhibited wrinkling of the glomerular capillary walls and a decrease in the glomerular tuft, which resulted in an increase in Bowman's space. There were also focal regions of cortical interstitial fibrosis and inflammation. QSM was able to detect negative and diffuse susceptibility values in the cortex, outer medulla and inner medulla. The negative susceptibilities indicate more diamagnetic materials in these regions. The diffuse and broad distribution indicates the diversity of magnetic material, microstructural heterogeneity and variation between animals in the *Agtr1a*−/− *Agtr1b*−/− cohort. This finding was consistent with the histology images and expected from an increase in pathological markers apparent in this model, e.g. fibrosis and inflammation. Fibrotic material, such as collagen, mostly comprises protein. Inflammation also generates numerous proteins and lipids. Proteins, lipids and certain mineralized tissues are very diamagnetic

(30,34). Although the QSM images were not able to resolve inflammation and fibrosis at the current image resolution, QSM determined the collective contribution of both inflammation and fibrosis. Finally, areas with diamagnetic susceptibilities are not exclusive to inflamed and fibrotic tissue. Other malformations with an abundance of extracellular matrix and nucleic acids, as an example, can exhibit diamagnetic susceptibilities (35–37). Further work is needed to characterize the magnetic susceptibilities of specific renal diseases and how to identify abnormalities in QSM images.

The isolated focal lesions of inflammation and fibrosis were closely associated with the major cortical vessels. Although these lesions were segmented using simple thresholding, other sophisticated algorithms can improve the segmentation and quantitatively determine the proximity of lesions to the major renal structures. The increase in inflammation and fibrosis and the associated susceptibility values are also related to the size of the major renal structures in addition to the proximity. From our results, we found that there were increased abnormalities in the knockout cohorts. Susceptibility values were more diamagnetic in these groups and were associated with areas of focal inflammation and fibrosis. Consequently, as these disease markers increased, the vessel segments and volumes of the renal regions decreased in the *Agtr1a*−/− and *Agtr1a*−/− *Agtr1b*−/− cohorts. One exception was the volume of the inner medulla, where no significant difference was found between the *Agtr1a*−/− and *Agtr1a*−/− *Agtr1b*−/− cohorts. Accordingly, the mean susceptibilities in the inner medulla were also not significantly different between the two knockout cohorts. The inner medulla was the only region to have approximately one-half of the volume in the two knockout cohorts compared with the wild-type, suggesting that the degree of inflammation and fibrosis, and thus greater diamagnetic susceptibility, may be related to the normal growth and development of the kidney tissue. In the AT_1-deficient model, the inner medulla is known to show the most hypoplasia, or underdevelopment.

We assumed the magnetic susceptibility to be scalar or isotropic in nature. The focal lesions, inflammation and fibrosis are areas with limited cellular arrangement and structural alignment and should not be anisotropic. For this reason, we focused mostly on the cortical architecture. In a normal kidney, the cellular arrangement and tissue microstructure of tubules and ducts may be more organized and anisotropic. The magnetic susceptibility of aligned parallel structures would depend on the orientation with respect to the external magnetic field and would require anisotropic or tensor-based susceptibility imaging (11,38,39). We have recently completed a study applying susceptibility tensor imaging of a normal kidney, and found anisotropy in the medullary regions and limited anisotropy in the cortical region (40). The susceptibility difference as a result of anisotropy was still much smaller than the baseline isotropic susceptibility difference in all three regions of the kidney. We expect anisotropy to be reduced in a mouse model with pathologies throughout the kidney.

In this study, we used a gadolinium contrast agent to stain the kidney. The introduction of the contrast agent shortened T_1 and T_2*, which allowed for shorter acquisition times and enhanced magnetic susceptibility contrast. The susceptibility values were different between the contrast- and noncontrast-enhanced kidneys. Nonetheless, in QSM MIP images, we found the same visible fine cortical structures with and without contrast agent in the kidneys from wild-type and *Agtr1a*−/− mice. In addition, the fine structures were less visible in *Agtr1a*−/− *Agtr1b*−/− mice with or without contrast agent. Furthermore, the mean susceptibility was more diamagnetic in the *Agtr1a*−/− and *Agtr1a*−/− *Agtr1b*−/− cohorts than in the wild-type cohort for both contrast- and noncontrast-enhanced kidneys. The susceptibility variation was consistently greater in the *Agtr1a*−/− *Agtr1b*−/− mice as a result of increased structural heterogeneity. With the introduction of the contrast agent, the contrast of susceptibilities increased with greater paramagnetic and diamagnetic values.

Although the contrast agent enhanced the magnetic susceptibility, more work is needed to understand the consequence of contrast addition and whether the compartmentalization of renal tubules affects the distribution of contrast agent and thus QSM values. Nevertheless, the qualitative evidence is clear that the small cortical abnormalities can be easily distinguished in MIPs from QSM images (both contrast- and noncontrast-enhanced kidneys) and not from magnitude images.

One limitation of our study is that the imaging protocols for kidneys with and without contrast agent are different. Kidneys without contrast agent had much longer T_1 and T_2* values and required longer TEs to obtain comparable magnetic susceptibility SNR. For this reason, we used a multiecho sequence, which has enhanced susceptibility SNR comparedwith a single echo sequence. To demonstrate, susceptibility values were measured at one echo from the multiecho dataset (shown in Tables S5 and S6). The measurements were taken at the fourth echo dataset (TE = 19.3 ms), which is near the T_2* value of the kidney and provides the optimal susceptibility SNR (28). The mean susceptibility values were similar to those of the multiecho-enhanced dataset; however, the standard deviations were much greater in the single echo dataset because of lower susceptibility SNR.

Another limitation is the relative nature of susceptibility values, which is a known and unresolved issue in QSM. In the present study, we measured susceptibilities in local regions of the kidney which were determined relative to those of the entire kidney. Ideally, susceptibilities should be measured relative to a large and separate homogeneous medium. For this reason, we also determined susceptibilities relative to the pelvis, which is a reasonably large and homogeneous structure separate from the major regions of the kidney. The local region measurements were determined far from the pelvis to avoid the detection of artificially ‘diamagnetic’ values because of the large dipole field generated by the strong paramagnetic content. Nonetheless, the values determined in this study are consistent with the increased pathology and heterogeneity in the different renal regions and disease cohorts. More work is needed to understand the influence of susceptibility values by factors such as contrast agent, pathology and QSM reconstruction.

We have demonstrated the utility of QSM to characterize inflammation and fibrosis in the kidney. Disease caused by fibrosis can be much more subtle in nature, but may be more indicative of renal disease than changes in the size of large structures. Various magnitude images have been used to identify fibrosis, including our own T_2*-weighted images; however, it can be challenging to identify focal lesions and to quantify small differences from these images. However, QSM demonstrated that it was able to enhance subtle differences in tissue architecture and to determine chemical composition, particularly in the cortex. This contrast mechanism is a very sensitive tool and can be applied to study (patho)physiology in a broader range of models. QSM can easily be extended to longitudinal imaging and may have diagnostic clinical applications for the detection of changes with disease or therapy.

The complete three-dimensional datasets and supporting information are available via CIVMSpace, our method for sharing information with the scientific community <http://www.civm.duhs.duke.edu/lx201204>.

Supplementary Material

Refer to Web version on PubMed Central for supplementary material.

Acknowledgments

The authors wish to thank Gary P. Cofer for technical assistance, Martin C. Fischer for microscopy and Sally Zimney for editorial assistance. The authors also wish to thank members of the Duke Center for In Vivo Microscopy for their discussions and contributions.

This work was supported by the National Institutes of Health/National Institute of Biomedical Imaging and Bioengineering (NIH/NIBIB) National Biomedical Technology Resource Center (P41 EB015897 to G.A.J.), NIBIB (T32 GM008555 to L.X.) and the National Institute of Diabetes and Digestive and Kidney Diseases (NIDDK) (R01 HL056122-14 to T.M.C.).

Abbreviations used

AT_1	angiotensin receptor type 1
AT_{1A}	angiotensin receptor type 1A
AT_{1B}	angiotensin receptor type 1B
H&E	hematoxylin and eosin
MIP	maximum intensity projection
QSM	quantitative susceptibility mapping
ROI	region of interest
SNR	signal-to-noise ratio

REFERENCES

1. Inoue T, Kozawa E, Okada H, Inukai K, Watanabe S, Kikuta T, Watanabe Y, Takenaka T, Katayama S, Tanaka J, Suzuki H. Noninvasive evaluation of kidney hypoxia and fibrosis using magnetic resonance imaging. J. Am. Soc Nephrol. 2011; 22:1429–1434. [PubMed: 21757771]
2. Nangaku M. Chronic hypoxia and tubulointerstitial injury: a final common pathway to end-stage renal failure. J. Am. Soc. Nephrol. 2006; 17:17–25. [PubMed: 16291837]
3. Bae KT, Grantham JJ. Imaging for the prognosis of autosomal dominant polycystic kidney disease. Nat. Rev. Nephrol. 2010; 6:96–106. [PubMed: 20111050]
4. Herget-Rosenthal S. Imaging techniques in the management of chronic kidney disease: current developments and future perspectives. Semin. Nephrol. 2011; 31:283–290. [PubMed: 21784277]
5. Pedrosa I, Alsop DC, Rofsky NM. Magnetic resonance imaging as a biomarker in renal cell carcinoma. Cancer. 2009; 115:2334–2345. [PubMed: 19402070]
6. Thoeny HC, Grenier N. Science to practice: can diffusion-weighted MR imaging findings be used as biomarkers to monitor the progression of renal fibrosis? Radiology. 2010; 255:667–668. [PubMed: 20501704]
7. Yanagita M. Inhibitors/antagonists of TGF-beta system in kidney fibrosis. Nephrol. Dial. Transplant. 2012; 27:3686–3691. [PubMed: 23114895]
8. Rauscher A, Barth M, Reichenbach JR, Stollberger R, Moser E. Automated unwrapping of MR phase images applied to BOLD MR-venography at 3 Tesla. J. Magn. Reson. Imaging. 2003; 18:175–180. [PubMed: 12884329]
9. Haacke EM, Xu Y, Cheng YC, Reichenbach JR. Susceptibility weighted imaging (SWI). Magn. Reson. Med. 2004; 52:612–618. [PubMed: 15334582]
10. Duyn JH, van Gelderen P, Li TQ, de Zwart JA, Koretsky AP, Fukunaga M. High-field MRI of brain cortical substructure based on signal phase. Proc. Natl. Acad. Sci. USA. 2007; 104:11 796–11 801.
11. Liu C. Susceptibility tensor imaging. Magn. Reson. Med. 2010; 63:1471–1477. [PubMed: 20512849]

12. Marques JP, Maddage R, Mlynarik V, Gruetter R. On the origin of the MR image phase contrast: an in vivo MR microscopy study of the rat brain at 14.1 T. Neuroimage. 2009; 46:345–352. [PubMed: 19254768]
13. de Rochefort L, Brown R, Prince MR, Wang Y. Quantitative MR susceptibility mapping using piece-wise constant regularized inversion of the magnetic field. Magn. Reson. Med. 2008; 60:1003–1009. [PubMed: 18816834]
14. de Rochefort L, Liu T, Kressler B, Liu J, Spincemaille P, Lebon V, Wu J, Wang Y. Quantitative susceptibility map reconstruction from MR phase data using bayesian regularization: validation and application to brain imaging. Magn. Reson. Med. 2010; 63:194–206. [PubMed: 19953507]
15. Li W, Wu B, Liu C. Quantitative susceptibility mapping of human brain reflects spatial variation in tissue composition. Neuroimage. 2011; 55:1645–1656. [PubMed: 21224002]
16. Liu T, Xu W, Spincemaille P, Avestimehr AS, Wang Y. Accuracy of the morphology enabled dipole inversion (MEDI) algorithm for quantitative susceptibility mapping in MRI. IEEE. Trans. Med. Imaging. 2012; 31:816–824. [PubMed: 22231170]
17. Shmueli K, de Zwart JA, van Gelderen P, Li TQ, Dodd SJ, Duyn JH. Magnetic susceptibility mapping of brain tissue in vivo using MRI phase data. Magn. Reson. Med. 2009; 62:1510–1522. [PubMed: 19859937]
18. Oliverio MI, Kim HS, Ito M, Le T, Audoly L, Best CF, Hiller S, Kluckman K, Maeda N, Smithies O, Coffman TM. Reduced growth, abnormal kidney structure, and type 2 (AT2) angiotensin receptor-mediated blood pressure regulation in mice lacking both AT1A and AT1B receptors for angiotensin II. Proc. Natl. Acad. Sci USA. 1998; 95:15 496–15 501.
19. Machura K, Steppan D, Neubauer B, Alenina N, Coffman TM, Facemire CS, Hilgers KF, Eckardt KU, Wagner C, Kurtz A. Developmental renin expression in mice with a defective renin–angiotensin system. Am. J. Physiol. Renal. Physiol. 2009; 297:F1371–F1380. [PubMed: 19710239]
20. Le TH, Oliverio MI, Kim HS, Salzler H, Dash RC, Howell DN, Smithies O, Bronson S, Coffman TM. A gammaGT-AT1A receptor transgene protects renal cortical structure in AT1 receptor-deficient mice. Physiol. Genomics. 2004; 18:290–298. [PubMed: 15306694]
21. Esther CR Jr, Howard TE, Marino EM, Goddard JM, Capecchi MR, Bernstein KE. Mice lacking angiotensin-converting enzyme have low blood pressure, renal pathology, and reduced male fertility. Lab. Invest. 1996; 74:953–965. [PubMed: 8642790]
22. Kim HS, Krege JH, Kluckman KD, Hagaman JR, Hodgin JB, Best CF, Jennette JC, Coffman TM, Maeda N, Smithies O. Genetic control of blood pressure and the angiotensinogen locus. Proc. Natl. Acad. Sci. USA. 1995; 92:2735–2739. [PubMed: 7708716]
23. Krege JH, John SW, Langenbach LL, Hodgin JB, Hagaman JR, Bachman ES, Jennette JC, O'Brien DA, Smithies O. Male–female differences in fertility and blood pressure in ACE-deficient mice. Nature. 1995; 375:146–148. [PubMed: 7753170]
24. Niimura F, Labosky PA, Kakuchi J, Okubo S, Yoshida H, Oikawa T, Ichiki T, Naftilan AJ, Fogo A, Inagami T. Gene targeting in mice reveals a requirement for angiotensin in the development and maintenance of kidney morphology and growth factor regulation. J. Clin. Invest. 1995; 96:2947–2954. [PubMed: 8675666]
25. Ito M, Oliverio MI, Mannon PJ, Best CF, Maeda N, Smithies O, Coffman TM. Regulation of blood pressure by the type 1A angiotensin II receptor gene. Proc. Natl. Acad. Sci. USA. 1995; 92:3521–3525. [PubMed: 7724593]
26. Johnson GA, Cofer GP, Gewalt SL, Hedlund LW. Morphologic phenotyping with magnetic resonance microscopy: the visible mouse. Radiology. 2002; 222:789–793. [PubMed: 11867802]
27. Johnson GA, Ali-Sharief A, Badea A, Brandenburg J, Cofer G, Fubara B, Gewalt S, Hedlund LW, Upchurch L. High-throughput morphologic phenotyping of the mouse brain with magnetic resonance histology. Neuroimage. 2007; 37:82–89. [PubMed: 17574443]
28. Wu B, Li W, Avram AV, Gho SM, Liu C. Fast and tissue-optimized mapping of magnetic susceptibility and T2* with multi-echo and multi-shot spirals. Neuroimage. 2012; 59:297–305. [PubMed: 21784162]
29. Schofield MA, Zhu Y. Fast phase unwrapping algorithm for interfero-metric applications. Opt. Lett. 2003; 28:1194–1196. [PubMed: 12885018]

30. Li W, Wu B, Avram AV, Liu C. Magnetic susceptibility anisotropy of human brain in vivo and its molecular underpinnings. Neuroimage. 2012; 59:2088–2097. [PubMed: 22036681]

31. Salomir R, De Senneville BD, Moonen CTW. A fast calculation method for magnetic field inhomogeneity due to an arbitrary distribution of bulk susceptibility. Concepts. Magn. Reson. B. 2003; 19B:26–34.

32. Liu C, Li W, Wu B, Jiang Y, Johnson GA. 3D fiber tractography with susceptibility tensor imaging. Neuroimage. 2012; 59:1290–1298. [PubMed: 21867759]

33. Xie L, Cianciolo RE, Hulette B, Lee HW, Qi Y, Cofer G, Johnson GA. Magnetic resonance histology of age-related nephropathy in the Sprague Dawley rat. Toxicol. Pathol. 2012; 40:764–778. [PubMed: 22504322]

34. Schweser F, Deistung A, Lehr BW, Reichenbach JR. Differentiation between diamagnetic and paramagnetic cerebral lesions based on magnetic susceptibility mapping. Med. Phys. 2010; 37:5165–5178. [PubMed: 21089750]

35. Maret G, Schickfus MV, Mayer A, Dransfeld K. Orientation of nucleic-acids in high magnetic-fields. Phys. Rev. Lett. 1975; 35:397–400.

36. Scholz F, Boroske E, Helfrich W. Magnetic anisotropy of lecithin membranes. A newanisotropy susceptometer. Biophys. J. 1984; 45:589–592. [PubMed: 6713071]

37. Torbet J. Fibrin assembly after fibrinopeptide A release in model systems and human plasma studied with magnetic birefringence. Biochem. J. 1987; 244:633–637. [PubMed: 3446182]

38. He X, Yablonskiy DA. Biophysical mechanisms of phase contrast in gradient echo MRI. Proc. Natl. Acad. Sci. USA. 2009; 106:13 558–13 563.

39. Lee J, Shmueli K, Fukunaga M, van Gelderen P, Merkle H, Silva AC, Duyn JH. Sensitivity of MRI resonance frequency to the orientation of brain tissue microstructure. Proc. Natl. Acad. Sci. USA. 2010; 107:5130–5135. [PubMed: 20202922]

40. Xie, L.; Dibb, R.; Li, W.; Liu, C.; Johnson, GA. Proceedings of the 21st Annual Meeting ISMRM. Vol. 23. Salt Lake City, UT, USA: 2013. Susceptibility tensor imaging of the renal tubule.

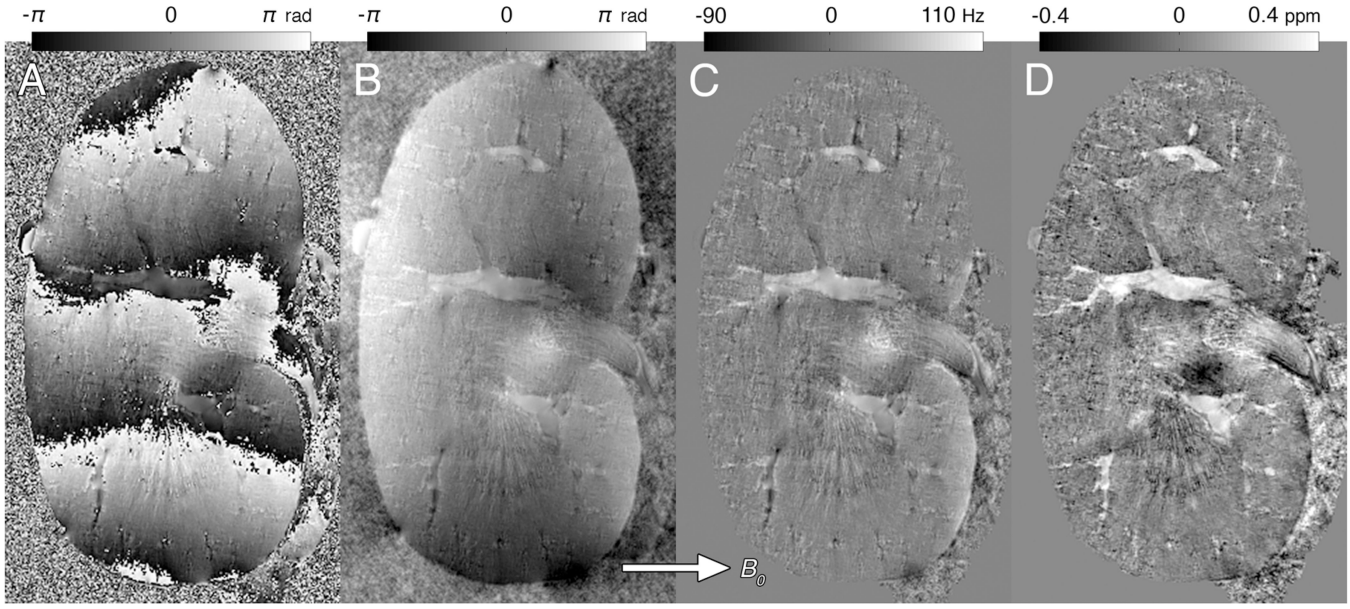

Figure 1.

Quantitative susceptibility mapping (QSM) reconstruction process for a kidney from a *Agtr1a*−/− mouse. (A) Phase from complex data. (B) Local phase extracted using Laplacian-based three-dimensional phase unwrapping. (C) Background phase removed using spherical-mean-value filtering. (D) QSM image computed by inverting the background-removed phase (least-squares algorithm using orthogonal and right triangular decomposition). Color bar: ppm of B_0.

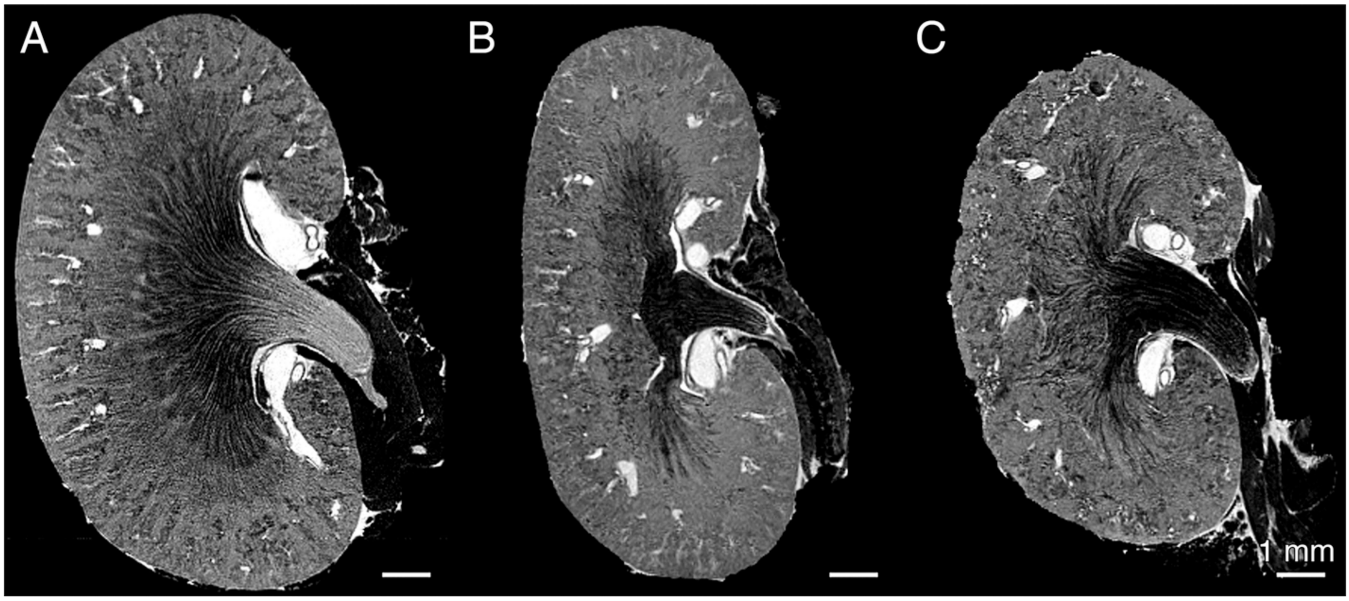

Figure 2.
MRI (T_1-weighted) coronal slices for kidneys from wild-type (A), *Agtr1a*−/− (B) and *Agtr1a* −/− *Agtr1b*−/− (C) mice. Oblique slices were chosen from the datasets to show all three regions of the kidney. Scale bars, 1 mm.

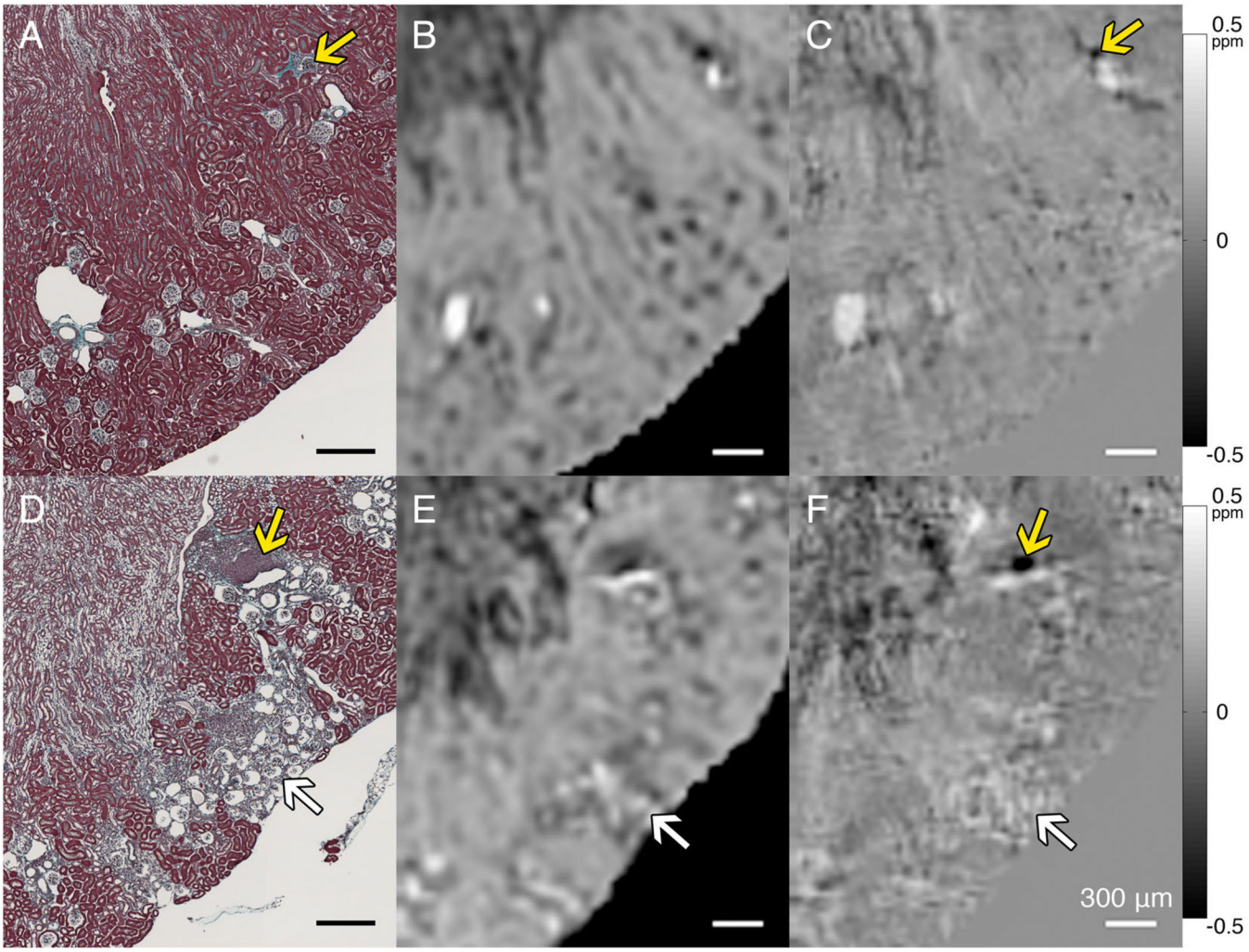

Figure 3.

Identification of cortical pathologies confirmed by Masson's Trichrome histology. Kidney images from wild-type (top row) and *Agtr1a*−/− *Agtr1b*−/− (bottom row) mice. (A, D) Histology images. (B, E) T_2*-weighted (magnitude) images. (C, F) Quantitative susceptibility mapping (QSM) images. Clusters of glomeruli with wall wrinkling can be seen (white arrows in D–F). The magnitude image shows susceptibility artifacts on the borders of the cluster. Focal regions of cortical interstitial inflammation and fibrosis were identified (yellow arrows in A, C, D and F). Scale bars, 300 µm. Color bar: ppm of B_0.

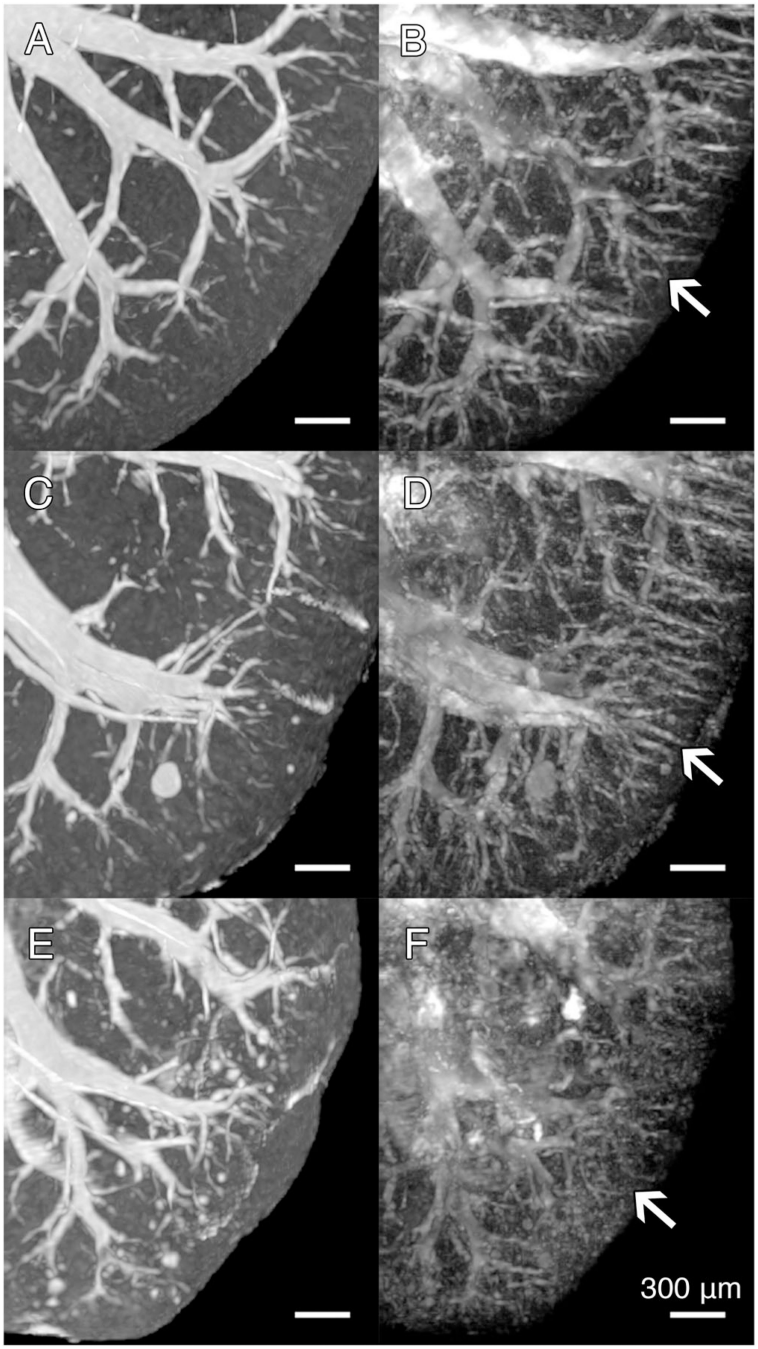

Figure 4.
Kidney images from wild-type (top row), *Agtr1a*−/− (middle row) and *Agtr1a*−/− *Agtr1b*−/− (bottom row) mice. MIPs from (A, C, E) T2* magnitude images. (B, D, F) MIPs from quantitative susceptibility mapping (QSM) images. White arrows point to structures in the most outer cortical region. Scale bars, 300 µm.

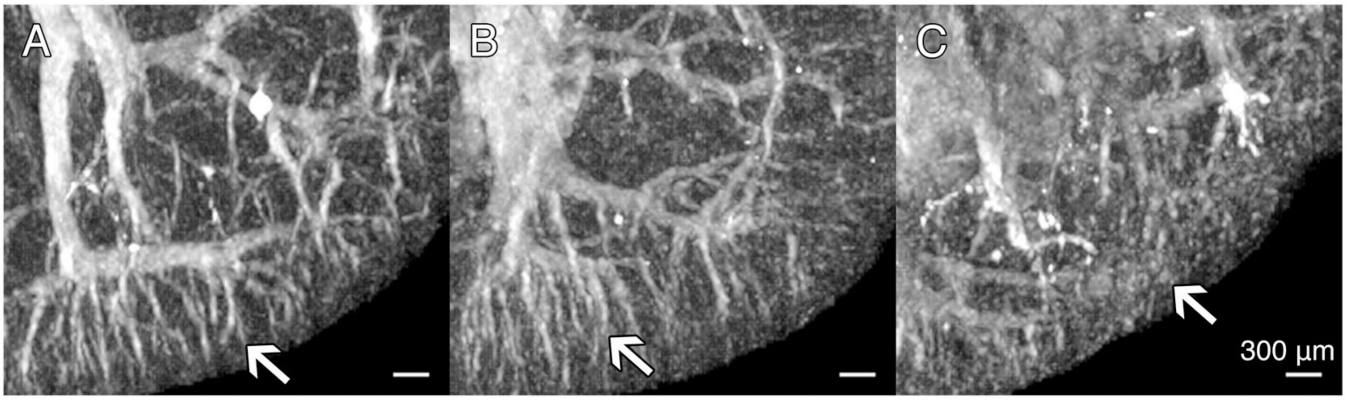

Figure 5.
Maximum intensity projections (MIPs) from quantitative susceptibility mapping (QSM) images of kidneys from wild-type (A), *Agtr1a*−/− (B) and *Agtr1a*−/− *Agtr1b*−/− (C) mice. White arrows point to structures in the most outer cortical region. These are kidneys without contrast agent. Scale bars, 300 μm.

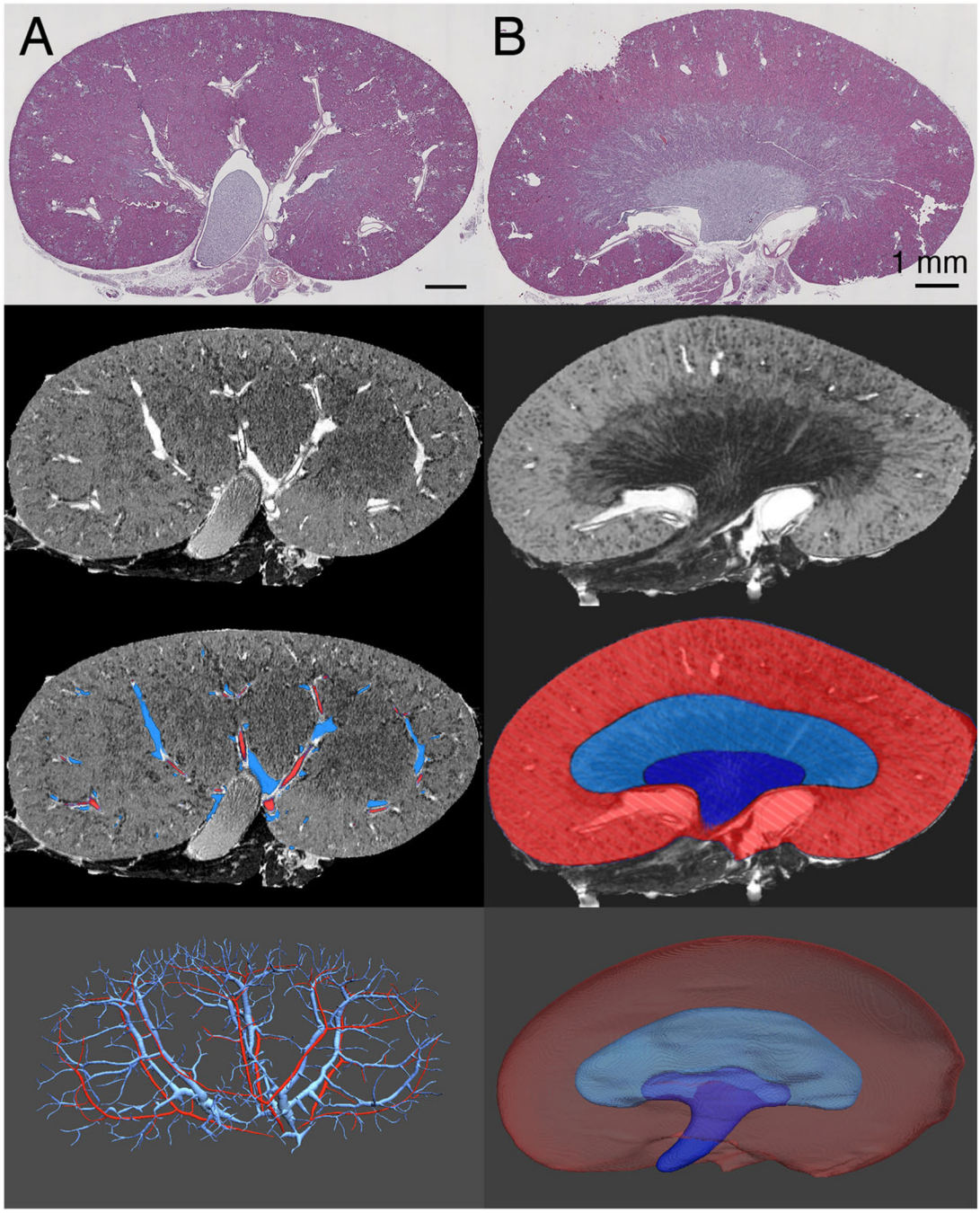

Figure 6.
Segmentation of renal structures confirmed by hematoxylin and eosin (H&E) histology. Images from wild-type mouse kidney. Top row: histology image. Second row: MR image. Third row: segmentation results overlaid on MR image. Bottom row: volume renders of the segmented structures. (A) Segmentation for the veins and arteries using T_1-weighted images. (B) Segmentation for the renal regions using T_2*-weighted images. Cortex shown in red, outer medulla shown in light blue and inner medulla shown in dark blue. Scale bars, 1 mm.

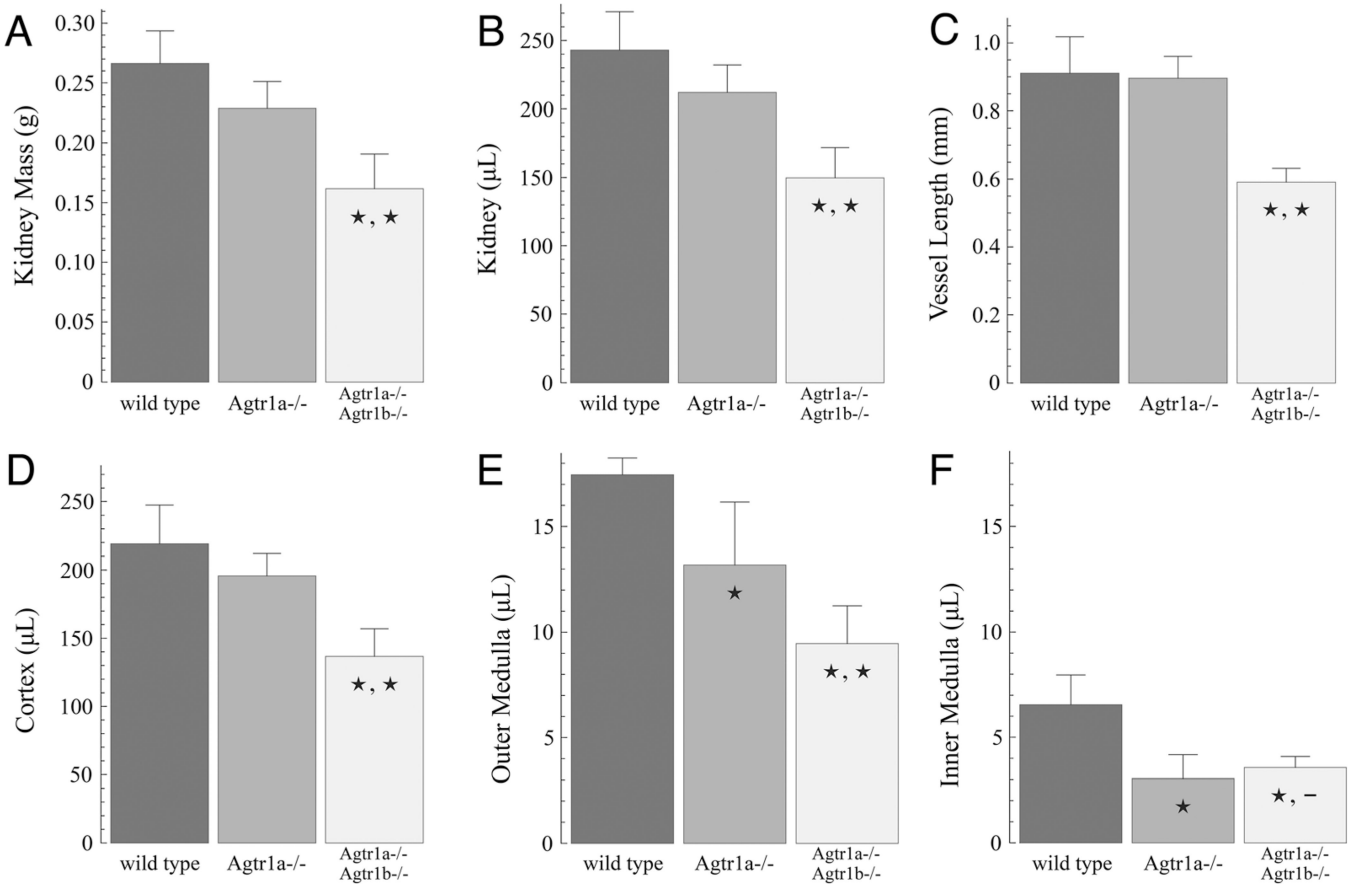

Figure 7.

Plots comparing kidneys from the three cohorts: (A) kidney mass; (B) total kidney volume; (C) mean vessel segment lengths (arterial); (D) cortex volume; (E) outer medulla volume; (F) inner medulla volume. *Significance between wild-type and *Agtr1a*−/− ($p < 0.05$). *,*Significance between wild-type and *Agtr1a*−/− *Agtr1b*−/−, and between *Agtr1a*−/− and *Agtr1a*−/− *Agtr1b*−/− ($p < 0.01$). *,¯Significance between wild-type and *Agtr1a*−/− *Agtr1b* −/− ($p < 0.01$) and no significance between *Agtr1a*−/− and *Agtr1a*−/− *Agtr1b*−/− ($p > 0.05$).

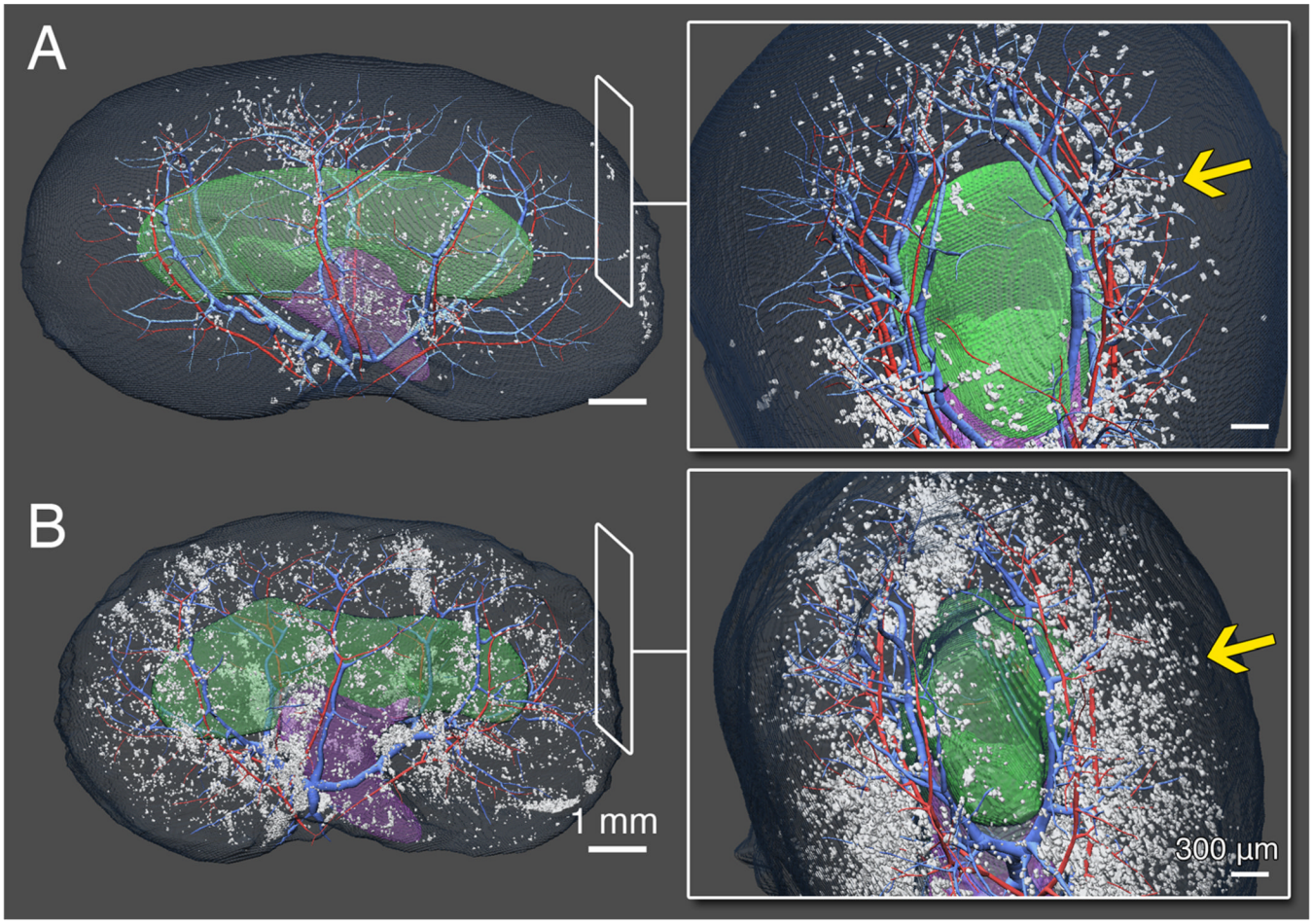

Figure 8.
Volume rendering of focal lesions of inflammation and fibrosis. Cortical lesions shown in relation to the vasculature and medullary regions. Kidneys from *Agtr1a*−/− (A) and *Agtr1a* −/− *Agtr1b*−/− (B) mice. Insets show a zoomed-in view of the cortex from an axial plane. The proximity of lesions to the vasculature and the extent of lesions in the cortex can be appreciated in the insets. Yellow arrows point to lesions. Inset scale bars, 300 μm. (A) and (B) scale bars, 1 mm.

Table 1

Relative quantitative susceptibility mapping (QSM) values in renal regions from kidneys with contrast agent

	χ (10^{-2} ppm)			
	Cortex	**Outer medulla**	**Inner medulla**	**Pelvis**
Wild-type (n = 4)	1.46 ± 0.36	2.14 ± 0.94	2.10 ± 2.80	39.62 ± 3.86
(relative to pelvis)	−38.16 ± 0.36	−37.48 ± 0.94	−37.52 ± 2.80	0 ± 3.86
Agtr1a−/− (n = 4)	−2.20 ± 0.68[a]	−6.21 ± 1.56[a]	−5.17 ± 3.67[a]	38.88 ± 2.64[b]
(relative to pelvis)	−41.08 ± 0.68[a]	−45.09 ± 1.56[a]	−44.05 ± 3.67[a]	0 ± 2.64[b]
Agtr1a−/− *Agtr1b*−/− (n = 6)	−7.68 ± 4.22[c]	−11.46 ± 2.13[c]	−7.57 ± 5.58[d]	40.50 ± 2.27[e]
(relative to pelvis)	−48.18 ± 4.22[c]	−51.96 ± 2.13[c]	−48.07 ± 5.58[d]	0 ± 2.27[e]

Mean χ ± standard deviation (SD). SD determined across tissue samples.

[a] Significance between wild-type and *Agtr1a*−/− ($p < 0.05$).

[b] No significance between wild-type and *Agtr1a*−/− ($p > 0.05$).

[c] Significance between wild-type and *Agtr1a*−/− *Agtr1b*−/−, and between *Agtr1a*−/− and *Agtr1a*−/− *Agtr1b*−/− ($p < 0.05$).

[d] Significance between wild-type and *Agtr1a*−/− *Agtr1b*−/− ($p < 0.05$) and no significance between *Agtr1a*−/− and *Agtr1a*−/− *Agtr1b*−/− ($p > 0.05$).

[e] No significance ($p > 0.05$).

Table 2

Relative quantitative susceptibility mapping (QSM) values in renal regions from kidneys without contrast agent

	χ (10^{-2} ppm)			
	Cortex	**Outer medulla**	**Inner medulla**	**Pelvis**
Wild-type (n = 1)	0.04 ± 1.10	0.67 ± 1.00	1.05 ± 0.59	4.90 ± 0.87
(relative to pelvis)	−4.86 ± 1.10	−4.23 ± 1.00	−3.85 ± 0.59	0 ± 0.87
Agtr1a−/− (n = 1)	−0.40 ± 1.20	−0.49 ± 0.91	−0.62 ± 0.71	4.78 ± 0.87
(relative to pelvis)	−5.18 ± 1.20	−5.27 ± 0.91	−5.40 ± 0.71	0 ± 0.87
Agtr1a−/− *Agtr1b*−/− (n = 1)	−0.60 ± 1.40	−0.74 ± 0.89	−0.80 ± 0.82	4.68 ± 1.22
(relative to pelvis)	−5.28 ± 1.40	−5.42 ± 0.89	−5.48 ± 0.82	0 ± 1.22

Mean χ ± standard deviation (SD). SD determined within region of interest (ROI) from a single kidney region.